GEOPHYSICS, VOL. 78, NO. 4 (JULY-AUGUST 2013); P. EN1–EN15, 7 FIGS., 2 TABLES.
10.1190/GEO2012-0395.1

A new coupled model for simulating the mapping of dense nonaqueous phase liquids using electrical resistivity tomography

Christopher Power[1], Jason I. Gerhard[1], Panagiotis Tsourlos[2], and Antonios Giannopoulos[3]

ABSTRACT

Electrical resistivity tomography (ERT) has, for a considerable length of time, been considered promising for subsurface characterization activities at sites contaminated with dense, nonaqueous phase liquids (DNAPLs). The relatively few field studies available exhibit mixed results, and the technique has not yet become a common tool for mapping such contaminants or tracking mass reduction during their remediation. To help address this, a novel, coupled DNAPL-ERT numerical model was developed that can provide a platform for the systematic evaluation of ERT under a wide range of realistic, field-scale subsurface environments. The coupled model integrated a 3D multiphase flow model, which generates realistic DNAPL scenarios, with a 3D ERT forward model to calculate the corresponding resistivity response. Central to the coupling, and a key contribution, was a new linkage between the main hydrogeologic parameters (including hydraulic permeability, porosity, clay content, groundwater salinity and temperature, and air, water, and DNAPL contents evolving with time) and the resulting bulk electrical resistivity by integration of a variety of published relationships. Sensitivity studies conducted for a single node compared well to published correlations and for a field-scale domain demonstrated that the model is robust and sensitive to heterogeneity in DNAPL distribution and soil structure. A field-scale simulation of a DNAPL release and its subsequent remediation, monitored by ERT surface surveys, demonstrated that ERT is promising for mapping DNAPL mass reduction. The developed model provides a cost-effective avenue to test optimum ERT data acquisition, inversion, and interpretative tools, which should assist in deploying ERT strategically at contaminated sites.

INTRODUCTION

Successful remediation of sites contaminated with dense nonaqueous phase liquids (DNAPLs) is a major challenge. DNAPLs are a class of industrial organic liquids, including chlorinated solvents, coal tar, and polychlorinated biphenyl oils, that are among the most hazardous and frequently detected contaminants detected in soil and groundwater (Kavanaugh et al., 2003). Upon release to the subsurface (e.g., due to rupture of a pipeline or tank), DNAPLs penetrate the pore space as an immiscible "oil" phase. With a density greater than water, DNAPLs routinely penetrate the water table and occupy the saturated zone. Their low solubility and high resistance to degradation relative to many groundwater contaminants means that a "DNAPL source zone" is typically expected to remain in the subsurface for decades, posing health risks to humans and ecosystems (Kueper et al., 2003).

Numerous studies have been conducted in recent years to understand the expected distribution of DNAPLs in the subsurface, including physical experiments at the bench (e.g., Illangasekare et al., 1995) and field scales (e.g., Kueper et al., 1993; Brewster et al., 1995), and numerical modeling studies (e.g., Dekker and Abriola, 2000; Gerhard and Kueper, 2003c). In fact, numerical models have become an essential tool for studying field-scale DNAPL behavior because field experiments are generally prohibited and laboratory experiments cannot reproduce the field-scale heterogeneity that is critical to DNAPL migration. From these studies, it is known that DNAPL source zones can exhibit a wide range of forms, from a laterally extensive layer near the surface (e.g., Gerhard et al., 2001) to a complex distribution of residual (trapped blobs) and pools (highly saturated accumulations) distributed widely and penetrating to significant depth (e.g., Gerhard et al.,

Manuscript received by the Editor 23 September 2012; revised manuscript received 24 January 2013; published online 4 June 2013.
[1]Western University, Department of Civil and Environmental Engineering, London, Ontario, Canada. E-mail: cpower9@uwo.ca; jgerhard@uwo.ca.
[2]Aristotle University of Thessaloniki, Department of Geophysics, Thessaloniki, Greece. E-mail: tsourlos@geo.auth.gr.
[3]The University of Edinburgh, School of Engineering, Edinburgh, UK. E-mail: a.giannopoulos@ed.ac.uk.

2007). The configuration of a particular DNAPL source zone is site specific and usually unknown in advance, because it depends on many complex factors including characteristics of the release and the detailed distribution of sands, silt, and clay lenses at the release location (Kueper and Gerhard, 1995; Gerhard et al., 2007).

Successful remediation of DNAPL sites depends on effective site investigation and monitoring strategies. Currently, DNAPL mapping typically relies on a sparse network of intrusive sample points (e.g., wells, cores, and test pits) that are costly and provide limited spatial and temporal resolution. Identifying the volume and distribution of soil impacted by DNAPL in this manner, initially and over time during remedial efforts, can be challenging because direct, conclusive evidence is often absent at most sampling locations (Kueper and Davies, 2009).

It has long been recognized that geophysical methods have the potential to significantly improve DNAPL site investigation and remediation monitoring (e.g., Brewster et al., 1995; Wilson et al., 2009). Electrical resistivity tomography (ERT), a well-established and widely used hydrogeophysics technique — e.g., for mapping moisture content (Zhou et al., 2001) and hydraulic conductivity (Slater, 2007) — is particularly promising because DNAPLs are typically much more resistive than groundwater (Lucius et al., 1992). The dissolved phase plume produced during natural dissolution of DNAPL is generally not considered of consequence for geoelectrical studies due to the small quantities of dissolved molecules (parts per million) and lack of charge carriers (organic molecules are electrically neutral) (e.g., Sauck et al., 1998; Redman, 2009). However, it is noted that, in some instances, chlorinated solvent plumes may exhibit increased electrical conductivity over time (e.g., Atekwana and Atekwana, 2009); this elevated conductivity has been attributed to increased dissolved ion concentrations in groundwater from mineral weathering occurring as a by-product of biodegradation of the dissolved solvent compounds (e.g., Sauck, 2000; Atekwana et al., 2005). In contrast, there is no evidence that the resistive nature of DNAPLs changes with time. Thus, a resistive DNAPL source zone beneath the water table presents a potential electrical target at sites whether or not significant dissolution or biodegradation is occurring.

The potential of ERT to detect DNAPL has been suggested by several controlled laboratory studies (e.g., Dhu and Heinson, 2004); for example, Chambers et al. (2004) use differential time-lapse resistivity imaging to monitor the movement of DNAPL through a saturated porous medium in a laboratory column. Applications at a handful of research sites have provided mixed results. Daily and Ramirez (1995) applied crosshole ERT at a chlorinated solvent site to track changes in resistivity associated with a subsurface remediation program that included the injection of an electron donor and infiltration of water. Newmark et al. (1998) use time-lapse crosshole resistivity images to monitor the removal of a mixed DNAPL during groundwater pumping. Cardarelli and Di Filippo (2009) use surface ERT with induced polarization (IP) to identify anomalies associated with the presence of DNAPL, whereas Chambers et al. (2010) use high-resolution, crosshole ERT in a pilot-scale experiment not to detect DNAPL directly but rather to map the groundwater chemistry changes associated with bioremediation.

ERT has not become a standard DNAPL site investigation tool due, in part, to the challenge of interpreting data from real contaminated sites. Most sites present a complex electrical target, including an unknown, often tortuous contaminant distribution superimposed upon an uncertain, heterogeneous distribution of soil properties. Moreover, unlike field experiments, real applications typically do not have the benefit of having a background image of the uncontaminated subsurface. It is not currently known under what circumstances ERT can be a valuable site investigation tool at DNAPL sites. It is expected that a range of scenarios exists for which ERT would be a cost-effective strategy, and this will be a function of (1) the degree of heterogeneity in the subsurface, (2) the depth and geometry of the DNAPL source zone, and (3) the extent of DNAPL mass removal during remediation. Moreover, this envelope of favorable conditions is likely dependent on the ERT survey design and processing methodology, neither of which have been optimized for DNAPL sites. It is possible that recent advances in ERT imaging (e.g., data acquisition and time-lapse monitoring) may be beneficial in this context (e.g., Ogilvy et al., 2009; Karaoulis et al., 2011a; Nenna et al., 2011). The systematic, controlled studies required to explore these questions at the field scale are not available from field trials or laboratory studies.

The objective of this study is to develop a numerical model able to determine the conditions under which ERT is able to map realistic DNAPL source zones within realistic subsurface environments at the field scale. This paper presents the development of such a model, which couples a simulator for DNAPL evolution under release and remediation conditions with a simulator for the corresponding ERT response of the subsurface. Central to the model coupling is the linking of hydrogeologic to geoelectric parameters, and presented is a sensitivity study to key elements of the chosen methodology. Finally, the paper presents the model's application to an example scenario. As a whole, the work provides a new, comprehensive model for ERT of DNAPL sites and demonstrates the potential of the model as a tool for better understanding the range of site conditions under which ERT may assist site remediation activities.

MODEL DEVELOPMENT

Model components

To simulate the electrical resistivity response of complex DNAPL architecture at the field scale, a novel coupling was developed between a model that simulates DNAPL contamination and remediation scenarios and one that simulates an ERT survey of the subsurface. Figure 1 highlights the key parameters that link the two models.

DNAPL3D-MT (Grant and Gerhard, 2007a, 2007b) is a 3D, finite-difference, multiphase flow model that is well established for simulating the migration and dissolution of DNAPL in heterogeneous porous media. The model solves the mass conservation equations for the simultaneous flow of DNAPL and groundwater; air is considered a passive phase at atmospheric pressure throughout the vadose zone. Implicit solution of these equations with Newton-Raphson iteration provides the distribution of hydraulic head and DNAPL saturation (i.e., the fraction of porosity occupied by DNAPL) throughout the domain at each time step. These, in turn, provide local values of groundwater velocity and DNAPL-groundwater interfacial area, which are integrated with the solution of the advection-dispersion equation to provide DNAPL dissolution rates and contaminant concentrations in groundwater. The model,

therefore, simulates a realistic initial distribution of DNAPL at a contaminated site and the complex pattern of DNAPL removal as it is dissolved by groundwater flowing through the site. (Complete details on the model formulation and solution methods are provided in Gerhard and Kueper, 2003a, 2003b, 2003c; Grant and Gerhard, 2007a, 2007b; Grant et al., 2007). The model has been used for numerous studies of DNAPL migration and dissolution at the field scale, including in 3D, heterogeneous domains (e.g., Alexandra et al., 2012). Although not considered for this work, the DNAPL model can also be used to investigate reactive transport processes, including chemical oxidation and bioremediation (e.g., West et al., 2008), and to simulate fractured-rock environments (e.g., Pang et al., 2007).

Whereas DNAPL3D-MT provides the distribution of DNAPL at each time step during the evolution of a contaminated site, an ERT model is used to simulate an ERT survey applied at the surface at regular intervals. Forward geoelectrical modeling was performed using a proven 3D algorithm that is fully described in Tsourlos and Ogilvy (1999). The forward model uses the finite element method to numerically solve Poisson's equation and mathematically predict the theoretical outcome (apparent resistivity) of a set of measurements from an ERT survey given a subsurface distribution of electrical resistivity. This particular forward modeling scheme has been used as a base in several modeling studies, including archeological investigations and salt tracer transport mapping (e.g., Papadopoulos et al., 2006, 2011; Karaoulis et al., 2011b).

As noted in Figure 1, the DNAPL model requires as input intrinsic hydraulic permeability (k) and total porosity (ϕ), defined at the same spatial resolution as the finite-difference grid. Heterogeneity of k, in particular, has long been known to be the dominant influence on the migration of DNAPL in soil and transport of dissolved contaminants in groundwater because k values naturally vary over at least nine orders of magnitude (e.g., Freeze and Cherry, 1979). In previous modeling with DNAPL3D-MT, the clay content was not explicitly identified; rather, its effects on DNAPL, groundwater, and aqueous contaminant movement were implicitly accounted for in soil properties such as k, ϕ, retardation coefficients, etc. However, explicit clay content is important in this context because the porosity, bound water, and specific surface area of the clay significantly affect the electrical properties of soil. Moreover, as illustrated in Figure 1, the spatial distributions of air, DNAPL, and water volumetric contents have a major influence on electrical resistivity (Archie, 1942). Therefore, central to linking the numerical models was establishing a reliable set of relationships that provides an electrical resistivity field (input parameter for the ERT forward model) that accounts for the spatial heterogeneity of subsurface soils (including clay) and the evolving spatial distributions of fluids in the soil porosity (air, DNAPL, and water).

Model linkage

The linkage methodology for this work is illustrated and detailed in Figure 2 and summarized in the following steps. Note that the methodology is described as applied to a single representative elementary volume of soil (i.e., single subsurface location, single node) but that it is applied to all locations in the domain simultaneously, once per time step.

Specify intrinsic hydraulic permeability

A random, spatially correlated, intrinsic hydraulic permeability field is generated to provide a realistic subsurface distribution of k. For this work, the field generator (FGEN) algorithm of Robin et al. (1991) was used because it has been demonstrated to avoid the diagonal artifacts found in other methods and has been used widely in hydrogeologic studies (e.g., Attinger et al., 2009; Alexandra et al., 2012). The value of k at each location is assumed to represent the total permeability resulting from a combination of clay and sand (volumetric fractions to be determined in subsequent steps).

Determine volumetric clay content

First, the lower threshold permeability of clean, clay-free sand, k_{sd}, is calculated (Revil and Cathles, 1999):

$$k_{sd} = \frac{d_{sd}^2 (\phi_{sd})^{3m_{sd}}}{24}, \tag{1}$$

where d_{sd} is the mean grain diameter of sand (m), ϕ_{sd} is the porosity of sand, and m_{sd} is the cementation exponent for sand. The values for these parameters are obtained from laboratory measurements and literature values. Note that k_{sd} is a single number for the entire domain and is invariant in time. For example, in this work, $d_{sd} = 2 \times 10^{-4}$ m, $\phi_{sd} = 0.32$, and $m_{sd} = 1.8$, which provides $k_{sd} = 3.6 \times 10^{-12}$ m^2, which corresponds to a fine sand. All k values greater than k_{sd} are taken as clay-free sand/gravel, whereas k values less than k_{sd} are indicative of sand containing a fraction of clay. It should be noted that k_{sd} can be determined using several methods, including laboratory and field measurements and empirical relationships such as the Kozeny-Carman equation (Bear, 1972).

Numerous studies of clay-sand mixtures have shown that an increase in clay content results in a decrease in permeability (e.g., Revil and Cathles, 1999; Schön and Georgi, 2003). Revil and Cathles (1999) develop an equation that determines the permeability of clay-sand mixtures as a function of volumetric clay content, and the porosities and permeabilities of pure sand and pure clay (the end members). Revil and Cathles (1999) demonstrated close agreement between predicted permeabilities and those measured over 11 orders of magnitude from available laboratory and core measurements. For this study, the equation by Revil and Cathles (1999) is rearranged to determine volumetric clay content Cl (ratio of clay, including water, to the whole soil volume) in terms of known parameters:

$$Cl = \frac{k_{sd}^{\frac{1}{3m_{cs}}} + k^{\frac{1}{3m_{cs}}}}{k_{sd}^{\frac{1}{3m_{cs}}} \left(\frac{1-\phi_{cl}}{\phi_{sd}}\right)}, \tag{2}$$

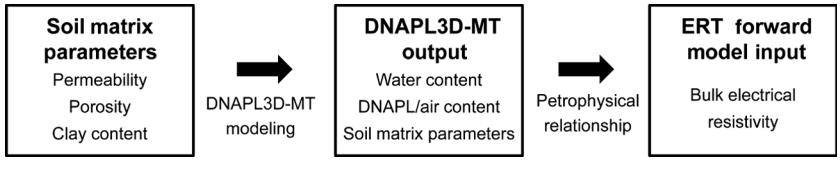

Figure 1. Schematic illustration of the parameters and steps considered during the coupled model development.

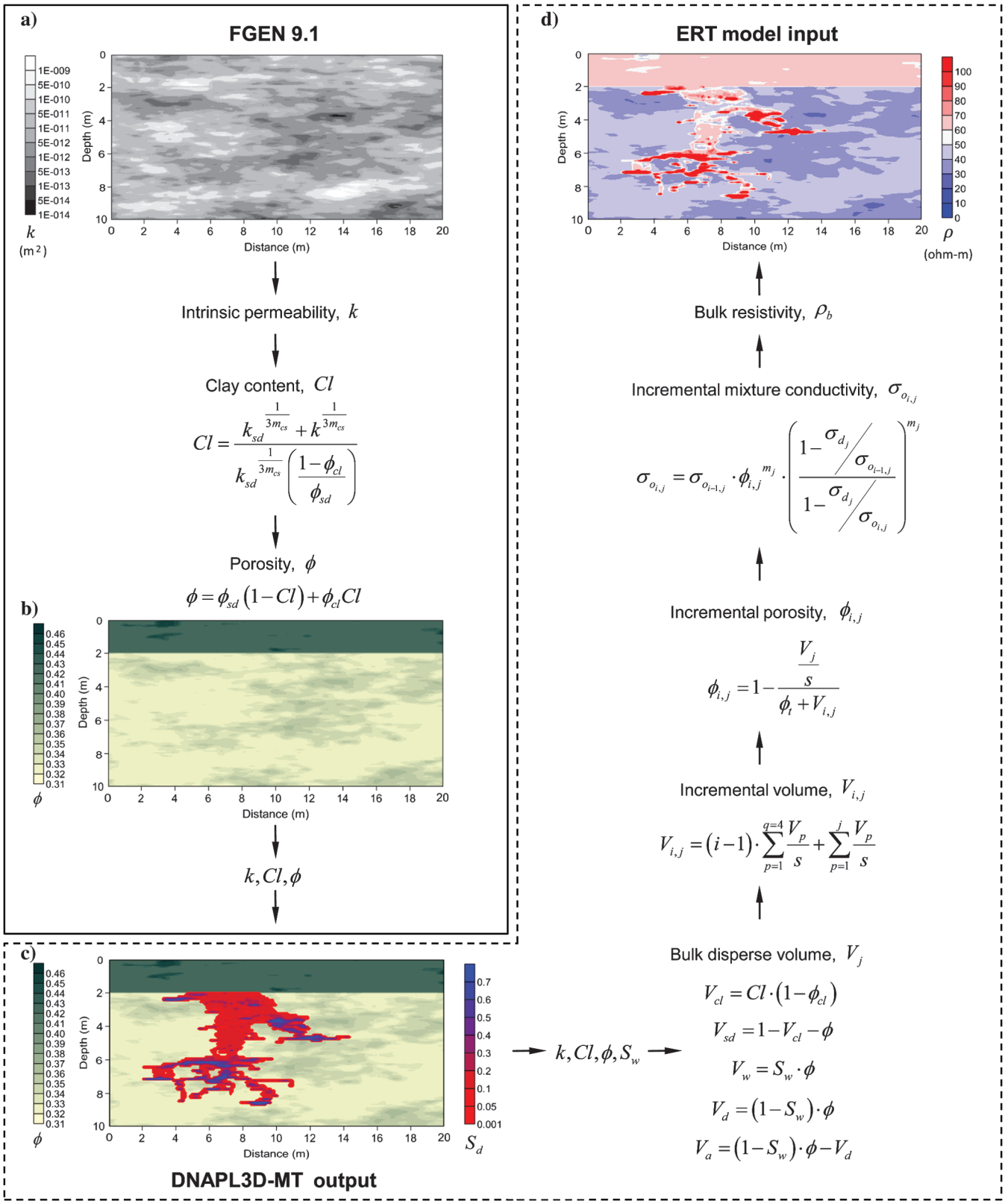

Figure 2. Schematic illustration of the methodology linking the multiphase flow model DNAPL3D-MT and the ERT forward model. The solid box encloses steps carried out once (at time = 0), whereas the dashed box encloses the linkage steps that are done repeatedly, once for each air/water/DNAPL configuration (i.e., at each time step). A full description of the equations and images shown is provided in the text.

where m_{cs} is the cementation exponent corresponding to the clayey sand domain and ϕ_{cl} is the porosity of pure clay. Equation 2 determines the volume of clay based on the sand/clay mixture permeability, k, and the threshold sand permeability, k_{sd}, computed in equation 1; for all locations where $k < k_{sd}$, the permeability is the result of a mixture of sand exhibiting a volume of clay Cl. Note that $Cl = 0$ for all nodes where $k > k_{sd}$. This model, with sand and clay coexisting at each macroscopic location, is valid as long as $Cl \leq \phi_{sd}$; this is representative of clayey-sand mixtures relevant to hydrogeologic studies (Giroux and Chouteau, 2008).

Determine total porosity and sand and clay volume fractions

The relationship between clay content and total porosity is influenced by the clay volume and its distribution within the porous matrix. Marion et al. (1992) derive a microgeometrical model based on adding clay such that it replaces sand porosity (i.e., pore-filling); the relationship for clay/sand mixtures exhibits a maximum clay content equal to the sand porosity and predicts decreasing electrical conductivity as clay content increases in a clayey sand (adding clay reduces total porosity). Alternatively, clay grains can be added in such a manner as to replace sand grains (e.g., de Lima and Sharma, 1990; Berg, 1995) such that total porosity is calculated:

$$\phi = \phi_{sd}(1 - Cl) + \phi_{cl}Cl. \tag{3}$$

Equation 3 exhibits the property that electrical conductivity increases as clay content increases, which matches expectations. Equation 3 has been used in numerous studies for incorporating clay fractions in predictions of electrical resistivity (e.g., de Lima and Sharma, 1990; Berg, 2007). It is therefore adopted here to compute total porosity at each location in the domain, and the subsurface volume comprising each fraction of the soil matrix at each location is then given by

$$V_{cl} = Cl \cdot (1 - \phi_{cl}), \tag{4}$$

$$V_{sd} = 1 - V_{cl} - \phi, \tag{5}$$

where V_{cl} is the volume fraction of clay and V_{sd} is the volume fraction of sand.

Determine volume fractions of DNAPL and water

At each time step, the DNAPL model solves for the fraction of pore space occupied by water, DNAPL and air. Therefore, the bulk volume occupied by each phase is

$$V_w = S_w \cdot \phi, \tag{6}$$

$$V_d = (1 - S_w) \cdot \phi, \tag{7}$$

$$V_a = (1 - S_w) \cdot \phi - V_d, \tag{8}$$

where V_w is the bulk water volume, V_d is the bulk DNAPL volume, V_a is the bulk air volume, and S_w is the water saturation (fraction of pore space containing water). It is noted that while steps 1–3 of this linking methodology are only executed once at the start of a new scenario, step 4 is conducted once per time step: after the DNAPL3D-MT model completes and before the ERT forward model is used.

Modify the pore water resistivity to account for salinity and temperature

The electrical resistivity of natural waters is dependent on the concentration and mobility of dissolved ions present in the pore fluid. The solution resistivity decreases with (1) increasing ionic concentrations, with pore-water resistivities ranging from ~100 for freshwater aquifers to ~0.5 ohm-m for salt water (e.g., Loke, 2010), and (2) increasing temperature because the ionic mobility and degree of dissociation are temperature dependent. The effect of ionic concentration and temperature upon the electrical resistivity of the pore water is accounted for by using the model of Sen and Goode (1992):

$$\rho_w = 1/\left[(5.6 + 0.27T - 1.5 \times 10^{-4}T^2) \cdot C_f - \left(\frac{2.36 + 0.099T}{1.0 + 0.214C_f}\right) \cdot C_f^{\frac{3}{2}}\right], \tag{9}$$

where T is the temperature (°C) and C_f is the ionic concentration (mol/L) associated with salinity. It is straightforward for the model to use alternative relationships between electrical resistivity of pore water and concentration of a wider range of ions (e.g., total dissolved solids, Schön, 1996). Thus, the model is well equipped to consider reactive transport processes that affect subsurface resistivity via dissolved ions such as biodegradation (e.g., Atekwana et al., 2005). This can be accomplished presently in an indirect manner by specifying elevated groundwater conductivity where the dissolved phase solvent is present or, in the future, directly by coupling biodegradation reactions in the plume to groundwater conductivity.

Determine overall resistivity

A variety of petrophysical relationships have been empirically and theoretically developed to relate electromagnetic to hydrogeologic properties. Differential effective medium theories, which are reviewed by Cosenza et al. (2009), provide a rigorous and widely used theoretical approach. Bruggeman (1935) and Hanai (1960, 1961) consider the macroscopic electrical properties of a heterogeneous mixture based on the properties of its components. The Hanai-Bruggeman (HB) equation for complex conductivity (electrical resistivity is described in this section in terms of its reciprocal, electrical conductivity) of a two-component mixture of matrix and water is (Bussian, 1983)

$$\phi = \left(\frac{\sigma_w^*}{\sigma_o^*}\right)^{\frac{(m-1)}{m}} \cdot \left(\frac{\sigma_o^* - \sigma_m^*}{\sigma_w^* - \sigma_m^*}\right), \tag{10}$$

where σ_w^* is the complex water (continuous phase) conductivity (S/m), σ_o^* is the complex mixture conductivity (S/m), σ_m^* is the complex matrix (disperse phase) conductivity (S/m), and m is the cementation exponent. At low frequencies (i.e., dc resistivity), the imaginary term of the complex conductivity is insignificant and the real conductivity can be used; therefore, the complex conductivity notation will be dropped for this study. The HB

equation is advantageous because (1) it reduces to Archie's law (Archie, 1942) at zero matrix conductivity, (2) it permits the inclusion of a conductive matrix, with some approaches also permitting a nonzero sand and nonzero hydrocarbon conductivity (e.g., Berg, 1995, 2007), and (3) it is formulated to handle frequency dependencies, complex conductivities and dielectric permittivities, which can be extended to study complementary geoelectrical techniques such as radar and spectral IP (e.g., Giroux and Chouteau, 2008; Revil, 2012).

Equation 10 has been the basis for several studies on the conductivity of clayey soils and rocks. Bussian (1983) develops a semiempirical saturation model to demonstrate the suitability of the HB equation for the study of conductivity in rocks at low frequencies, but it is approximated for a limited range of conditions. de Lima and Sharma (1990) use a first-principle approach to develop a model for adding clay and sand grains in small, but proportional, amounts; however, it limits the cementation exponents for each component to a value of 1.5. Berg (1995) uses volumetric-weighted averaging to associate hydrocarbons, in addition to the composite matrix (sand and clay) grains, with the disperse phase component of the HB equation. The main limitation of this particular model is that the host water must have a much higher conductivity than the matrix and hydrocarbons; this may be true at high salinities, but the accuracy of the approach may be affected at low water salinities and saturations (Berg, 2007). Revil et al. (1998) use the model by Bussian (1983) to account, in a more sophisticated way, for the surface conductivity of the electrical double layer at the grain/water interface; however, several complex electrochemical variables were used and other studies treat surface conductance as an equivalent clay volume conductance (e.g., de Lima and Sharma, 1990). Berg (2007) presents a dispersed-clay algorithmic approach that accommodates simultaneous mixing of any number of disperse elements and is applicable to all frequencies, salinities, and conductivities. This "incremental" model uses discrete integration of the HB calculation to add tiny, but proportional, amounts of disperse elements into the disperse phase (matrix) component, including clay, sand, and hydrocarbons (Berg, 2007). This method overcomes order-of-addition problems associated with several disperse components while also accommodating independent exponents for each disperse phase and their associated conductivities. Berg (2007) demonstrates that the model works well on experimental data under a wide range of conditions and produces results very close to the results from other published models (e.g., Waxman and Smits, 1968; Bussian, 1983; de Lima and Sharma, 1990).

The incremental model by Berg (2007) was selected for this work because it is the most versatile and applicable to the wide range of conditions that are typically present in aquifers of primary interest in DNAPL studies. The disperse element associated with hydrocarbons in Berg (2007) will be used to account for the DNAPL and air components in this model. In the iterative inclusion process, the calculated mixture conductivity from the current iteration constitutes the fluid conductivity for the next iteration. The volumes for the four disperse elements (clay, sand, DNAPL, and air) are divided into equal portions for each increment s. The disperse volume sum at each step is given by (Berg, 2007)

$$V_{i,j} = (i-1)\cdot \sum_{p=1}^{q=4} \frac{V_{\mathrm{P}}}{s} + \sum_{p=1}^{j} \frac{V_{\mathrm{P}}}{s}, \tag{11}$$

where $V_{i,j}$ is the volume sum at increment i and disperse element j, q is the number of disperse elements ($q = 4$), and V_{P} is the bulk volume of each respective disperse element j. The porosity for each increment i at disperse element j is then given by (Berg, 2007)

$$\phi_{i,j} = 1 - \frac{\frac{V_j}{s}}{\phi_t + V_{i,j}}, \tag{12}$$

where V_j is the bulk volume of disperse element j and ϕ_t is the total water volume ($\phi_t = S_w \cdot \phi$). The routine to calculate each incremental σ_o is based on equation 10, which can be rearranged as

$$\sigma_{o_{i,j}} = \sigma_{o_{i-1,j}} \cdot \phi_{i,j}^{m_j} \cdot \left(\frac{1 - \sigma_{d_j}/\sigma_{o_{i-1,j}}}{1 - \sigma_{d_j}/\sigma_{o_{i,j}}} \right)^{m_j}, \tag{13}$$

where $\sigma_{o_{i,j}}$ is the electrical conductivity of the mixture at increment i and disperse element j, $\sigma_{o_{i-1,j}}$ is the electrical conductivity of the mixture of the previous increment that becomes the fluid conductivity for the current iteration, σ_{d_j} is the electrical conductivity of disperse element j, and m_j is the exponent related to disperse element j (cementation exponents m_{sd} and m_{cl} used for sand and clay inclusions, respectively, and saturation exponent n used for DNAPL and air inclusions). The routine computing equation 13 is called $s \cdot q$ times, and each time the small volume portions are added to the mix. The "final" incremental σ_o at increment s and disperse element q provides the overall bulk electrical conductivity of the heterogeneous mixture. This is computed once per time step, after DNAPL3D-MT has provided the fluid saturation values, and before the ERT forward model is used.

The linkage methodology described in steps 1–6 was written in MATLAB code that efficiently combined the FGEN, DNAPL3D-MT, and ERT models. Solving the HB routine in equation 13 for σ_o at each increment was accomplished using the Newton-Raphson technique for finding roots. The number of increments s was set to 100 because this provides sufficient accuracy (Berg, 2007). Effective medium models have a tendency to calculate different mixture conductivities depending on the order that the disperse elements are added; reversing the order of input of the disperse elements on each successive step of the incremental method overcomes this problem and further improves accuracy (Berg, 2007).

Sensitivity analysis

The linkage methodology presented in this paper accounts for several hydrogeologic and electric parameters, each exhibiting an influence on the generated bulk electrical resistivity. Here, the sensitivity of predicted resistivity is considered as a function of assumptions used in the model, first at the scale of a single node and then at the scale of an entire domain. Figure 3a plots the predicted bulk resistivity value of a single node as a function of DNAPL saturation and clay content (see curves labeled "Berg [2007]", presenting calculations with equations 11–13 of the presented model). The node considered is below the water table, where $S_w + S_d = 1$. The figure illustrates that, as expected, bulk resistivity increases with increasing DNAPL saturation, with the sensitivity becoming more pronounced as DNAPL saturation increases beyond 50%. Moreover, as expected, the addition of conductive clay decreases predicted resistivity. The presence of significant amounts

of clay reduces the sensitivity to DNAPL saturation in the region $S_d > 50\%$ because this corresponds to low water content, and thus the relative contribution of clay to the bulk resistivity is higher. A variety of geochemical processes and in situ conditions can influence the resistivity of groundwater. Figure 3b illustrates the sensitivity of predicted bulk resistivity to the assumed resistivity of groundwater and clay content in the absence of DNAPL. As expected, higher resistivity groundwater corresponds to increased bulk resistivity in the model. However, here too, the sensitivity is diminished with increasing clay content.

In addition, Figure 3 compares this sensitivity of the presented model with that achieved when other formulations are used in place of equations 11–13 (i.e., Waxman and Smits, 1968; de Lima and Sharma, 1990; Berg, 1995). It is evident that this model produces similar results to alternative models for the parameters used. The models are indistinguishable for the case of zero clay in Figure 3a and 3b. Increased clay fractions produce some differences in the predicted bulk resistivity at very high DNAPL saturations (Figure 3a) and high water resistivities (Figure 3b); this is expected as these conditions approach or exceed the limiting condition implicit in the de Lima and Sharma (1990, equation 18) and Berg (1995) models, which requires the water resistivity to be much less than the matrix resistivity. It is noted that equation 13, used for this study, does not exhibit the same limitation.

To consider the model sensitivity at the domain scale, a DNAPL release scenario was simulated in a 2D domain 20×10 m deep, with a nodal spacing of 0.1 m in each direction resulting in 20,000 nodes. The k-field was generated with a mean k of 8.91×10^{-11} m^2 (mean $\ln(k) = -25.4$ m^2), variance $\ln(k) = 2.97$, and an exponential autocorrelation structure of 5.0 m horizontally and 0.5 m vertically; the distribution of k for the single realization used is illustrated in Figure 2a (gray-scale image where darker shades of gray correspond to lower permeability). Considering the saturated zone (20×8 m deep, 16,000 nodes), the distribution of k values is illustrated by the histogram shown in Figure 4a. As discussed earlier, all k values less than the sand permeability threshold correspond to clay-containing soil (equation 1); here, $k_{sd} = 3.6 \times 10^{-12}$ m^2 and Figure 4a illustrates that this corresponds to 4913 nodes (31%) for this k-field. Figure 4b shows the corresponding distribution of clay content in the domain (equation 2), with 4913 nodes exhibiting $Cl > 0$ (mean $Cl = 0.09$, max $Cl = 0.32$). The distribution of total porosity is plotted in Figure 4c, illustrating that total porosity is equal to sand porosity at the 11,087 nodes containing zero clay and total porosity increases with increasing clay content (equation 3). The spatial distribution of porosity is illustrated in Figure 2b (green scale with darker shades corresponding to higher clay content), revealing that higher clay content regions correspond to the low permeability lenses of Figure 2a.

The permeability, clay content, and total porosity fields constitute the soil matrix domain into which a 1 m^2 release of trichloroethylene (TCE) DNAPL (a common subsurface contaminant) was simulated. Figure 2c presents the spatial distribution of the DNAPL 10 days after the release, at which time the DNAPL has formed a complex source zone. As expected, DNAPL primarily occupies the higher permeability regions (i.e., low clay content) because these represent the least resistive flow pathways. Figure 4d demonstrates that the DNAPL occupies 2313 nodes (14%) and exhibits saturations from 1% to 94% of the pore space (mean $S_d = 25\%$).

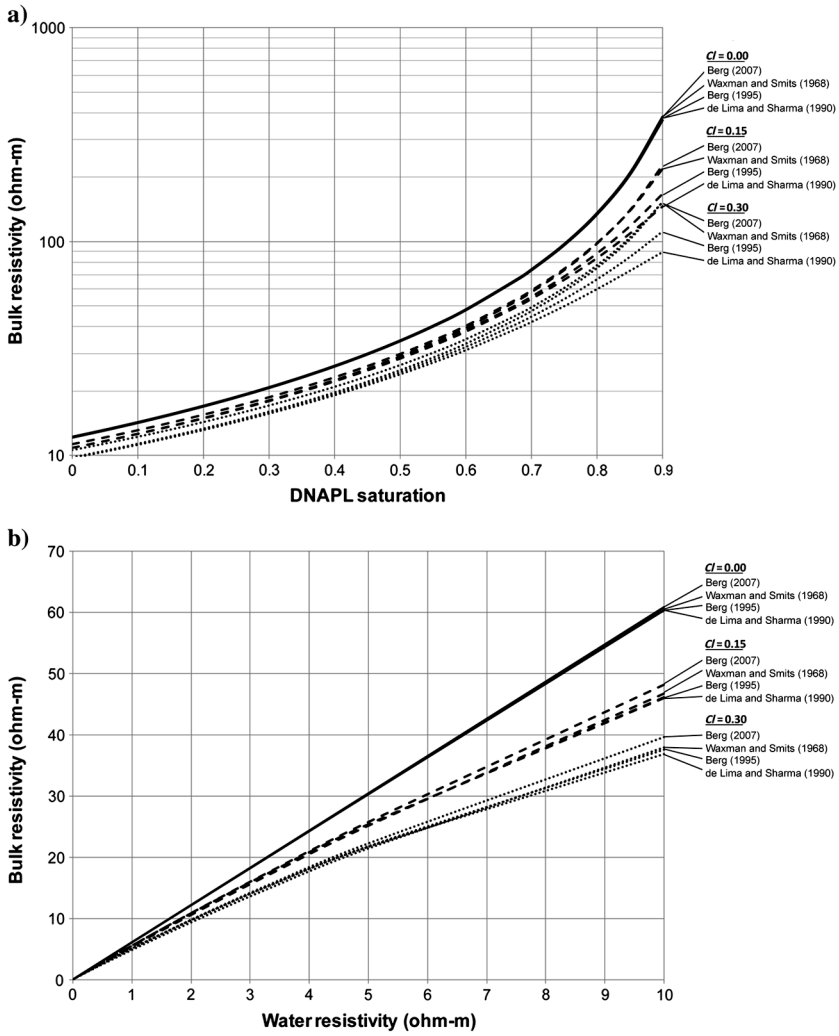

Figure 3. Bulk resistivity variation with (a) DNAPL saturation and (b) water resistivity, as a function of clay content ($Cl = 0.0$, solid line; $Cl = 0.15$, dashed line; $Cl = 0.3$, dotted line). Model used in this paper (Berg [2007], see equations 11–13) compared with other published models. The input variables were $\rho_w = 2$ ohm-m (a), $\rho_{cl} = 40$ ohm-m, $\rho_{sd} = 1000$ ohm-m, $\rho_d = 1.79 \times 10^{11}$ ohm-m (Brewster and Annan, 1994), $m_{sd} = m_{cl} = 1.5$, $S_d = 0.0$ (b), $\phi_{sd} = 0.30$ and $\phi_{cl} = 0.40$; values selected to meet the constraints of the other petrophysical models (i.e., exponents = 1.5 for equation 18 of de Lima and Sharma [1990], $\rho_w < \rho_{cl}/\rho_{sd}/\rho_d$ for de Lima and Sharma [1990]; Berg [1995]). The cation exchange capacity of clay for Waxman and Smits (1968) comparison = 0.03 meq/g (i.e., kaolinite). Note that the vertical axis of (a) uses a logarithmic scale.

As illustrated in Figure 2, in order for the model to predict bulk resistivity at each node, it is necessary to specify the concentration of ions in groundwater and the resistivity of the DNAPL; in this example, values of 900 ppm (e.g., Giroux and Chouteau, 2008) and 1.79×10^{11} ohm-m (e.g., Brewster and Annan, 1994) were used. Figure 5a reveals that the predicted bulk resistivities for the soil matrix only ranges from 48.17 (clay-free soil) to 30.61 ohm-m ($Cl = 0.3$) (mean = 46.3 ohm-m). It further demonstrates that the presence of the DNAPL source zone (Figure 2c) results, as expected, in a wider distribution of predicted values, ranging from 4228.7 ($Cl = 0.0$, $S_d = 0.94$) to 30.6 ohm-m (mean = 58.7 ohm-m). The predicted spatial distribution of bulk resistivity is provided in Figure 2d, in which the strong contrast between the DNAPL and the background is evident; in addition, the variability predicted within the soil matrix is clear.

The sensitivity of the predicted bulk resistivity field to several key model parameters was investigated. Figure 5b again presents the distribution of resistivities related to the base case (DNAPL = 1.79×10^{11} ohm-m, ionic concentration in water = 900 ppm), and compares it to the case of a less resistive DNAPL (DNAPL = 30 ohm-m, ionic concentration = 900 ppm). It is evident that, as expected, the most significant influence is on the upper limit of predicted bulk resistivity values (i.e., highest DNAPL saturations), which reduced from 4228.7 to 406.4 ohm-m; less impact is observed in the middle range, while, of course, no change is observed in DNAPL-free soil, resulting overall in a decrease in the mean bulk resistivity from 58.7 to 49.6 ohm-m. A second comparison is made against a case in which the concentration of ions in the groundwater was decreased (DNAPL = 1.79×10^{11} ohm-m, ionic concentration = 450 ppm), thereby increasing the groundwater resistivity. Figure 5b illustrates that this resulted, as expected, in increased predicted resistivity values at all locations, with the range becoming 6208.3 to 51.1 ohm-m and the mean increasing from 58.7 to 111.7 ohm-m. It is evident from the variations in the distribution of resistivities that the coupled model is handling changes in key model parameters as expected.

DEMONSTRATION SIMULATION

DNAPL spill scenario

A field-scale contamination scenario was simulated in a 3D model domain with a surface area of 12 m long (x-direction) by 12 m wide (y-direction), and a depth of 4 m (z-direction). The domain was discretized into 73,728 nodes with a nodal spacing of

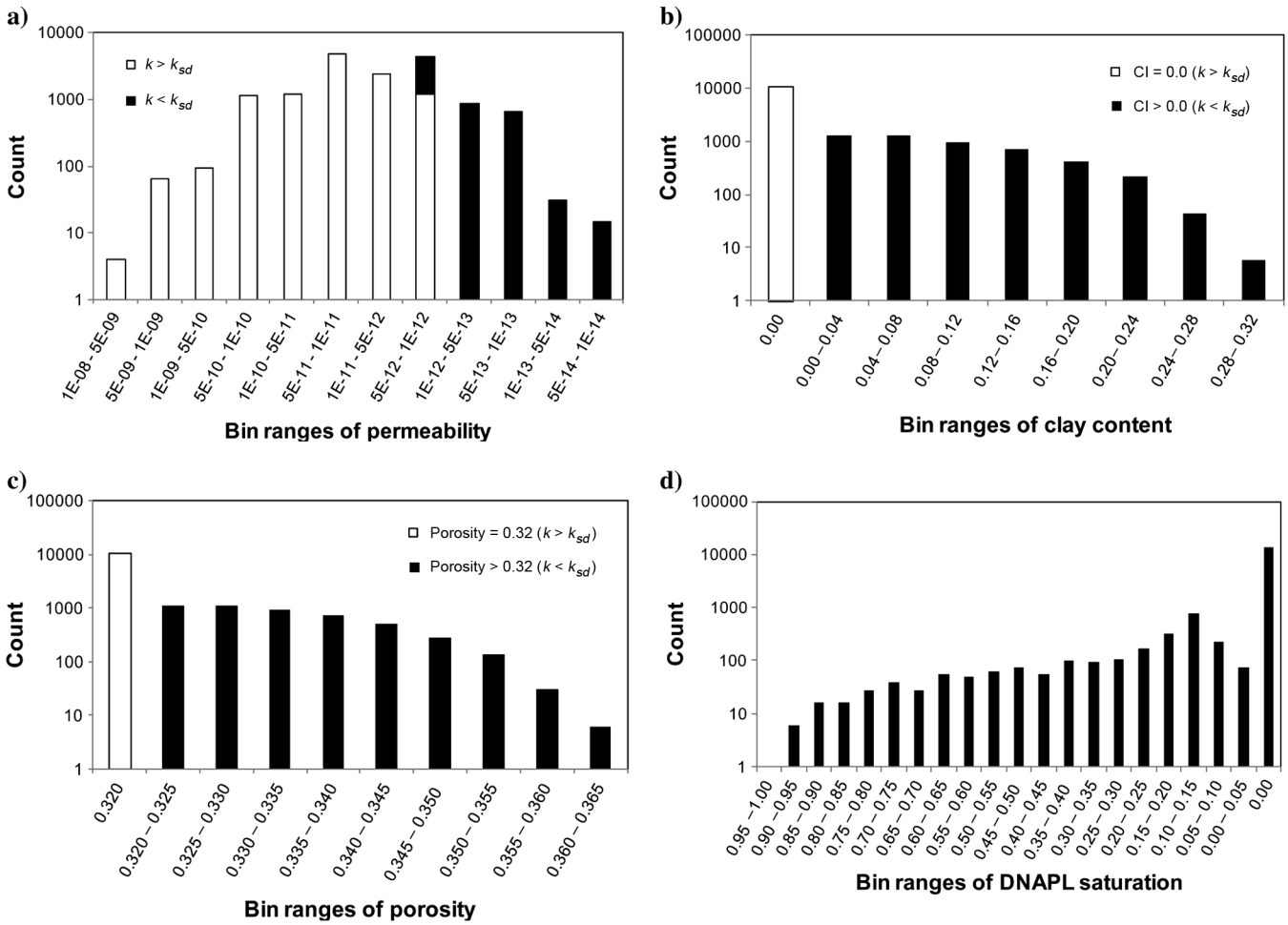

Figure 4. Histograms illustrating the distributions of the key model parameters for all of the nodes in the saturated zone for the example model domain illustrated in Figure 2: (a) intrinsic hydraulic permeability, (b) clay content, (c) total porosity, (d) DNAPL saturation values at $t = 10$ days. In all cases, counts are presented on a logarithmic axis.

0.250 m in the x- and y-directions and 0.125 m in the z-direction. The domain used a random, spatially correlated, k field generated using FGEN to represent the heterogeneous subsurface. The permeability generator used an exponential autocorrelation function with the statistics provided in Table 1, based on an aquifer in Canada on which a detailed geostatistical analysis was conducted (Sudicky et al., 2010). The corresponding clay content and total porosity at each node was determined from the presented linkage methodology (equations 2–3). A total of 26% (19,063 nodes) were determined to exhibit $Cl > 0$, with a mean $Cl = 0.08$ and variance of $Cl = 0.003$. For the entire domain, the mean total porosity = 0.33 and the variance of porosity = 0.001. The result was a domain with unconsolidated porous media dominated by horizontal lenses exhibiting a distribution of permeability, porosity, and clay content representative of an aquifer characterized, on average, by a medium sand and encompassing soils ranging from clay to gravel.

The water table was established at 0.250 m below the ground surface, below which the domain was initially fully saturated with water ($S_w = 1$). Above the water table, the domain was partially saturated ($S_w = 0.7$). The near-surface soils in the vadose zone contained higher porosity and smaller particle sizes than deeper soils (e.g., Revil and Cathles, 1999). In this simulation, the capillary fringe is assumed to be negligible; although it is acknowledged that explicitly incorporating a capillary fringe may provide a more gradual transition in electrical properties, it is not expected to significantly impact the conclusions of this work. The side boundaries were characterized by fixed, hydrostatic water pressures that established an ambient hydraulic gradient of 0.01 from left to right across the domain, and the bottom boundary was set as impermeable to DNAPL and water.

The release of a chlorinated solvent DNAPL commonly found at contaminated sites, 1,1 dichloroethylene (1,1 DCE) (note that TCE was used in the sensitivity analysis above), was simulated through a 1.0 m^2 patch area located centrally in the domain (in plan view) and located coincident with the water table. Table 1 provides the fluid properties used. The aim was to mimic a leaking underground storage tank or the bottom of a waste lagoon. To achieve this in the model, a constant DNAPL flux was assigned to each node within the patch area, with the value assigned weighted according to the node's k and ensuring the sum achieved a total flux of 1.3 m^3/day (Grant et al., 2007). The source was initiated at time $t = 0$ and was turned off at $t = 1$ day, representing the release of 1.3 m^3 (1300 l) of DNAPL. To achieve a realistic initial distribution of DNAPL in the subsurface, the DNAPL was allowed to continue to migrate under gravity and capillary forces for six days after the source was turned off. During this time, no DNAPL was permitted to dissolve and, at t = 7 days — coinciding with the start of the ERT survey — the resulting DNAPL distribution was "immobilized" so that no further DNAPL migration occurred. The purpose of this modeling step was (1) to ensure that the full 1300 l was retained as the initial DNAPL volume and (2) to ensure that the only signal available for subsequent geophysical detection was DNAPL disappearance. These simplifying assumptions are reasonable considering the focus of this paper is on demonstrating a DNAPL-ERT resistivity model linkage. Note that a subsequent publication will focus on using the developed model to evaluate the ability of ERT to track DNAPL remediation for a range of DNAPL release scenarios, soil types, and soil distributions.

At t = 7 days, DNAPL dissolution was enabled, and the simulation was then continued until $t = 1.3$ years, by which time all of the released DNAPL mass had dissolved into the ambient groundwater flowing through the source zone. It is acknowledged that 1,1 DCE has a relatively high solubility in groundwater (Table 1), and complete natural dissolution of a DNAPL source zone could require decades (Kueper et al., 2003). Engineered remediation of DNAPL source zones, however, can substantially accelerate DNAPL mass removal rates. The rate of mass removal is independent of the objectives of this work.

The electrical properties assigned to each soil and fluid constituent are presented in Table 2. In this study, the pore water was at a temperature of 20 °C and composed of Na^+ and Cl^- ions at 900-ppm concentration, which is within the range usually characterized as fresh water. The resistivity values assigned to each soil type are assumed to be independent of temperature variations. The resistivity of clay could be calculated to account for the surface conductivity at the grain water interface (e.g., Revil et al., 1998);

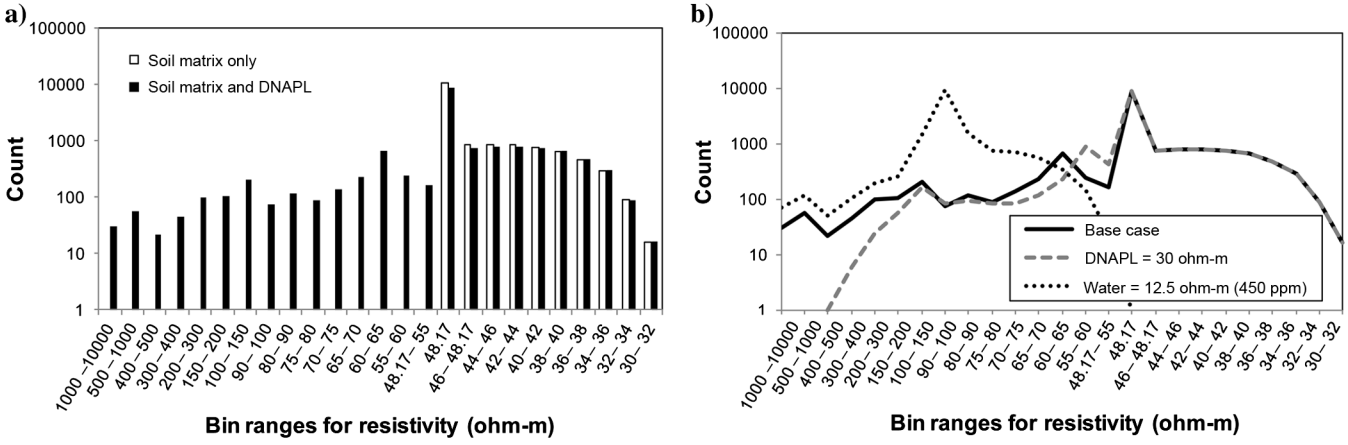

Figure 5. Histograms of predicted resistivity values for the saturated zone of the example model domain presented in Figure 2: (a) soil matrix only (white bars) versus soil matrix plus DNAPL (black bars), (b) soil matrix plus DNAPL (black line; identical to black bars in 5a) for base case (DNAPL = 1.79×10^{11} ohm-m, ionic concentration in water = 900 ppm) compared to case with less resistive DNAPL (dashed gray line; DNAPL = 30 ohm-m, ionic concentration = 900 ppm) and case with increased water resistivity (dotted black line; DNAPL = 1.79×10^{11} ohm-m, ionic concentration = 450 ppm).

however, for this demonstration, an equivalent clay volume conductance is obtained from the literature.

ERT modeling and inversion

Site investigation and remediation of DNAPL sites invariably begins subsequent to a known or discovered release. For this study, it was assumed that site investigation by ERT was initiated at $t = 7$ days. ERT surveys were simulated at intervals corresponding to 10% reductions of DNAPL mass to obtain 10 time-lapsed images of the site remediation during the source zone life span (corresponding to $t = 9$, 15, 24, 35, 50, 72, 100, 144, 226, 474 days). The geoelectrical modeling finite-element mesh, using hexahedral elements, was designed with the same resolution as the DNAPL model finite-difference grid, thereby permitting the underlying hydrogeologic parameters of the latter to be directly assigned 1:1 (i.e., no interpolation necessary) as a total resistivity value to each finite element block (as determined by the linkage methodology described in equations 1 through 13). Each 3D ERT survey was simulated using dense, parallel survey lines traversing only in the x-direction (e.g., Papadopoulos et al., 2006, 2007); the pole-dipole configuration in a combined forward and reverse mode (A-MN and NM-A) was used, with an inline electrode spacing of 0.5 m (25 electrodes along each survey line) and an interline spacing of 0.5 m (25 survey lines). Furthermore, to render modeling results more realistic, random noise with a Gaussian distribution of 3-mV/A peak-to-peak amplitude was added to the synthetic potential difference data.

An inversion model is required to invert the (observed) apparent resistivity values to obtain the "true" subsurface resistivity distribution. The ERT inversion program DC_3DPro (Yi et al., 2001; Kim and Yi, 2010) was used for this study; DC_3DPro performs 3D, iterative smoothness constrained inversion and uses the active constraint balancing technique to efficiently calculate the Lagrangian multiplier vector for each iteration (Yi et al., 2003). Independent inversion of each ERT survey was used. Future work will consider a detailed study of time-lapse monitoring and the optimal array configuration, inversion algorithm, and processing methodology for tracking DNAPL remediation.

Table 1. Hydrogeologic parameters.

Parameter	Value	Units
Mean (lnk)[4]	−25.4	m^2
Variance (lnk)[4]	1.94	—
Correlation lengths[4]	4.0 (horizontal); 0.5 (vertical)	m
Sand porosity[5]	0.32 (saturated); 0.46 (vadose)	—
Clay porosity[5]	0.42 (sat); 0.56 (vad)	—
Sand particle diam. [5]	2.0×10^{-4} (sat); 6.0×10^{-5} (vad)	m
Water density[6]	1000	kg/m^3
Water viscosity[6]	0.001	$Pa \cdot s$
DNAPL density[6]	1170	kg/m^3
DNAPL viscosity[6]	0.0005	$Pa \cdot s$
DNAPL solubility[7]	5.1	kg/m^3
Interfacial tension[7]	0.04	N/m

[4]Grant and Gerhard (2007).
[5]Bear (1972).
[6]Gerhard et al. (2007).
[7]Mercer and Cohen (1990).

Table 2. Electrical parameters.

Parameter	Value	Units
Water resistivity[8]	6.5	ohm-m
DNAPL resistivity[9]	1.79×10^{11}	ohm-m
Air resistivity[9]	1.79×10^{11}	ohm-m
Sand resistivity[10]	500	ohm-m
Clay resistivity[10]	30	—
Saturation exponent[11]	2.0	—
Cementation exponent of sand[12]	1.8	—
Cementation exponent of clay[12]	2.7	—

[8]Calculated from equation 9 in this paper.
[9]Brewster and Annan (1994).
[10]Loke (2010).
[11]Berg (2007).
[12]Revil and Cathles (1999).

ERT detection of DNAPL source zone

Figure 6a illustrates the 3D hydrogeologic model domain at the start of the ERT investigation (i.e., 100% DNAPL remaining), while Figure 6c and 6e shows cross-sectional and plan-view images of the subsurface, respectively. The figure reveals that DNAPL has penetrated to a 3-m depth in the subsurface and spread to cover an area approximately 4×4 m in the plan view. The DNAPL is observed to consist of a complex network of pools and residual, exhibiting a range of DNAPL saturations from 1% to 74% of the pore space. Three distinct pools of high-DNAPL saturation exist at 0.5-, 1.5-, and 2.5-m depths (see Figure 6c), hereafter named pool 1, pool 2, and pool 3, respectively. Qualitative consideration of the corresponding true (inverted) resistivity distribution (see Figure 6b, 6d, and 6f) suggests that the combined DNAPL-ERT simulation produced realistic ERT images of (1) the subsurface heterogeneity and (2) the DNAPL body.

In Figure 6b, the higher resistivity (red), near-surface response corresponds to the vadose zone. Notice that within the vadose zone, there happened to exist a lower resistivity (blue) region corresponding to the higher porosity (and higher clay content) region shown in Figure 6a (dark green). The hydrogeologic and resistivity plan-view images at 0.5-m depth (section A-A) presented in Figure 6e and 6f, respectively, again demonstrate that the soil matrix variability is realistically simulated in the ERT response; for example, the lowest resistivities (dark-blue) in Figure 6f correspond to higher clay contents associated with the lowest permeabilities (dark-gray) in Figure 6e. Figure 6c and 6d, which presents the cross-sectional images at 6 m in the y-direction (section B-B), reveals that the ERT response reasonably accounts for the soil matrix variability in the near-surface soil (top 1 m), but it is unable to detect variability at larger depths, which is expected because ERT sensitivity reduces with depth.

The strongest contrasts in the ERT response are representative of the water-DNAPL distinction, and it is evident that the DNAPL distribution is reasonably imaged by the simulated ERT survey. For example, the true resistivity distribution in Figure 6d indicates two distinct zones of high resistivity (red) at depth intervals of 0.2–0.5 and 1.0–2.5 m, respectively. These zones correspond to the DNAPL pools: ERT resolved pool 1 from pool 2, but was unable to resolve the deeper pool 3, instead enveloping pool 2 and pool 3. This is expected due to the reduced sensitivity of ERT with depth and the fact that shallow targets can interfere with the detection of deeper targets. Thus, it is not surprising that the detailed distribution of pools characteristic of a complex DNAPL may be challenging to resolve. Several methods can be used to provide optimum subsurface information, including informed ERT survey design (e.g., Nenna et al., 2011), and future work will explore these techniques in the context of DNAPL investigations. However, overall, Figure 6 suggests that, at favorable sites, ERT may be suitable for determining the outer boundaries of the location and depth of a DNAPL

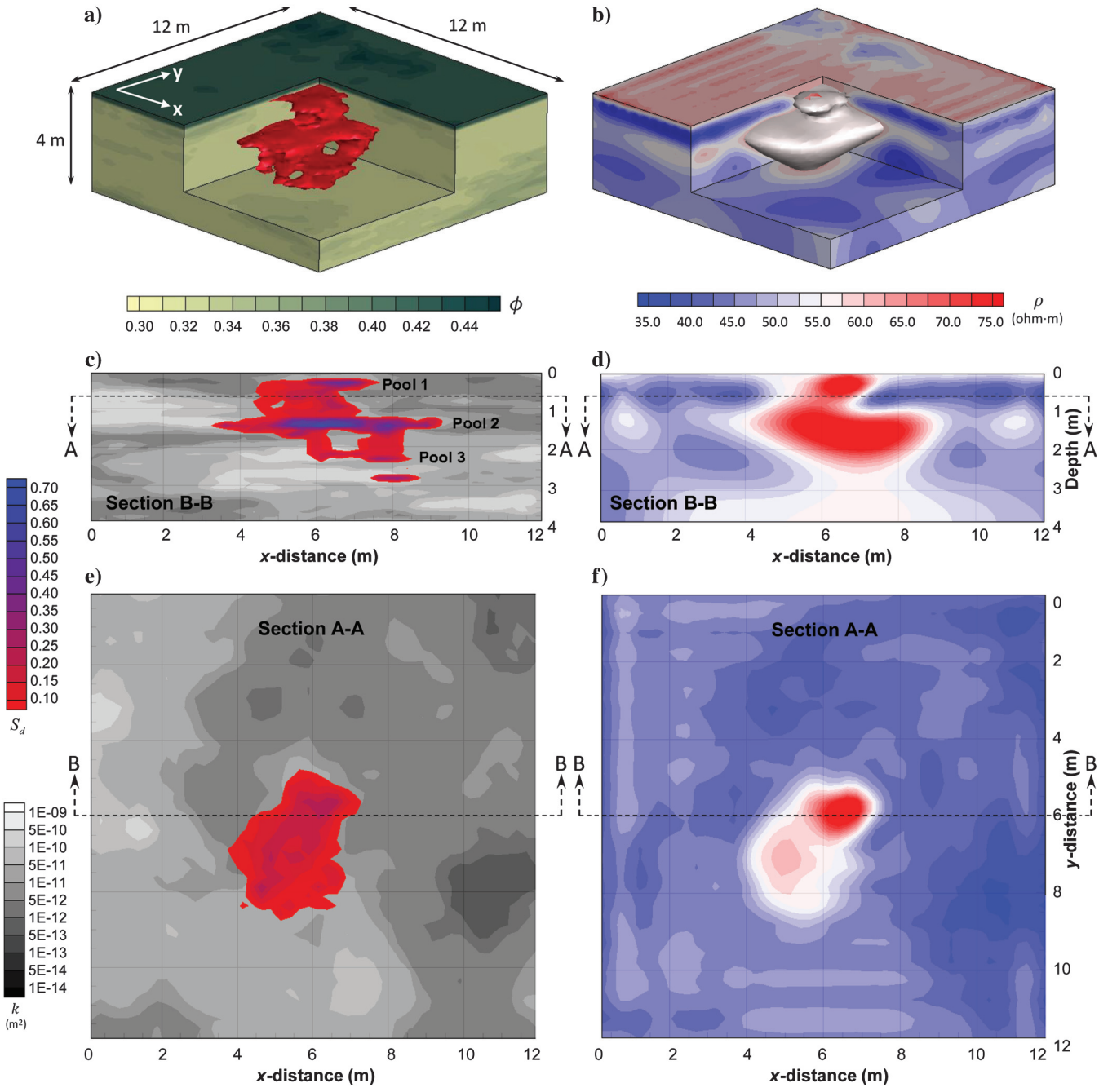

Figure 6. Field scenario 7 days after DNAPL release: (a) 10% DNAPL saturation isosurface, (b) 56 ohm-m resistivity isosurface, (c, e) DNAPL saturation distribution in cross section and plan view, and (d, f) corresponding resistivity distribution. A threshold DNAPL saturation of 10% corresponds to a threshold resistivity of 56 ohm-m, as determined by the linkage model.

body in heterogeneous porous media, with increased resolution toward the surface as expected.

Mapping DNAPL remediation

It is acknowledged that several factors may change the magnitude of the DNAPL signal relative to the background, including an increase in the soil matrix heterogeneity and clay content and evolving resistivity of the DNAPL plume (e.g., enhanced conductivity due to biodegradation). However, time-lapse monitoring of DNAPL remediation may remain promising even in such scenarios because the background heterogeneity is constant and the evolving signal directly corresponds to changes in DNAPL mass and distribution. As mentioned, ERT surveys were simulated at intervals corresponding to ~10% reductions of the DNAPL mass. Although difference or 4D inversion routines (e.g., Kim et al., 2009; Karaoulis et al., 2011a) may best take advantage of the differences detected, such optimization of the ERT analysis for DNAPL remediation is the subject of future work.

Figure 7a and 7c reveals that, as expected, the DNAPL mass was removed from the source zone in a heterogeneous manner (compare to Figure 6c). For example, most of the residual DNAPL was dissolved first, as is common (e.g., Grant and Gerhard, 2007b). As well, pool 3 disappeared relatively early because it resided in a relatively high permeability zone that experienced significant groundwater flux. With 58% of the DNAPL removed, the remaining source zone was dominated by pools 1 and 2. Figure 7b and 7d reveals that the ERT response changed correspondingly to the mass reduction of DNAPL. In fact, because the parts of the source zone first remediated were, coincidentally, the low saturations and the deepest pool (i.e., the DNAPL that was the least well resolved by ERT), the inverted images became more effective at characterizing the source zone during remediation. Although it is not possible to extrapolate generally based on a single case, and the fortuitous removal of the deepest pool will not always occur, it is generally true that DNAPL source zone geometry simplifies with time and becomes characterized by isolated, substantial DNAPL pools. This may lead to continual improvement of the ERT response as remediation progresses. Overall, this work suggests that ERT may be promising in revealing reductions in DNAPL mass over time.

DISCUSSION

The coupled multiphase-geophysics numerical model presented is able to account for various hydrogeophysical parameters, including groundwater quality (e.g., salinity, temperature), soil matrix (e.g., heterogeneity, clay content), and electrical (e.g., conductivities, survey design, inversions) properties. This universal linkage model permits simultaneous mixing of any number of disperse elements and accommodates geometric factors, such as sand and clay porosity exponents and saturation exponents, for each disperse element and its associated resistivity. In addition, the model can handle complex conductivities and complex dielectric permittivities, which may permit future modeling work on complementary geoelectrical methods (e.g., spectral IP and ground-penetrating radar).

A sensitivity analysis of the predicted bulk resistivity, conducted at the scale of a single location and an entire domain, provided

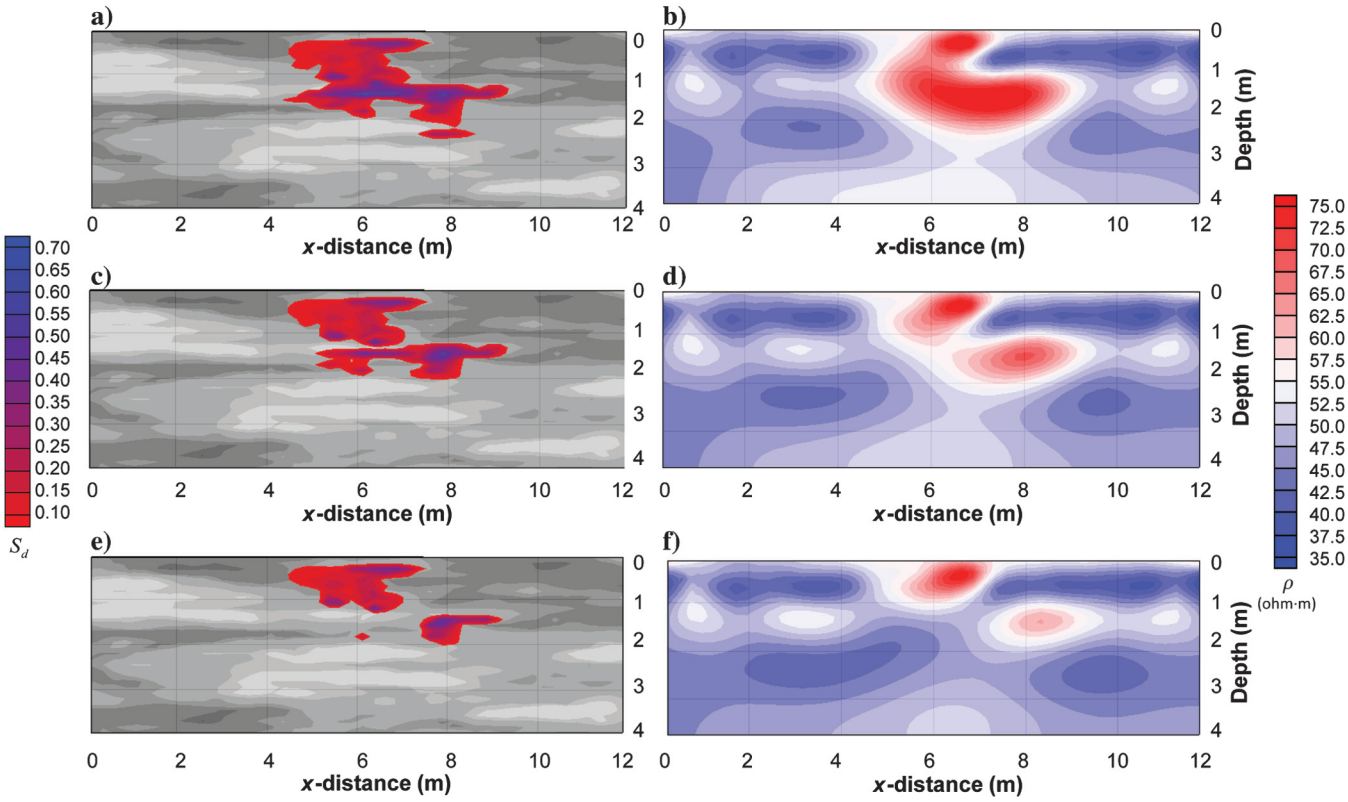

Figure 7. Cross section of spill scenario after (a) 28%, and (c) 58%, and (e) 78% of the original DNAPL mass has been removed and the corresponding resistivity distribution after (b) 28%, (d) 58%, and (f) 78% of the DNAPL mass has been removed.

confidence in the linkage methodology presented. As expected, bulk resistivity increases with (1) increasing DNAPL saturation, (2) higher resistivity groundwater (corresponding to reduced groundwater salinity), and (3) reduced clay fraction. Furthermore, the relative contribution of clay to the bulk resistivity is higher in regions of high DNAPL saturation and/or high water resistivity. Analysis of the model sensitivity for a 2D case demonstrated that a realistic distribution and correlation of hydrogeologic parameters, including hydraulic permeability, clay content, and porosity, were generated and (with the addition of the DNAPL distribution) subsequently mapped to a realistic distribution of bulk electrical resistivity. The presented model was demonstrated to provide a good match to other published models across a range of key parameters within the bounds to which those other models can be applied. However, the presented model can also be applied outside these bounds and can work at all water salinities and tool frequencies.

A 3D, field-scale, surface release of a chlorinated solvent DNAPL into heterogeneous clayey sand, including complete DNAPL remediation and its mapping by time-lapsed surface ERT surveys, demonstrated realistic ERT responses that were sensitive to heterogeneity in soil properties and DNAPL saturations. Although static detection of the initial DNAPL distribution appears possible under ideal circumstances, it is expected to be challenging in most sites due to the difficulty in distinguishing these two complex signals. However, the simulated ERT response appears sensitive to changes in the mass and distribution of DNAPL, suggesting that ERT has the potential for tracking the time-lapsed remediation of a DNAPL source zone. Such a noninvasive tool, which could map where and how quickly DNAPL mass changes with time during site cleanup, would be a major step forward in remediation practice.

Several simplifying assumptions in the demonstration case were used for the purposes of this initial, exploratory work. The water table was relatively shallow for an unconfined aquifer and contained moderate water saturations with no capillary fringe effects. A resistive DNAPL was assumed in the presence of groundwater exhibiting constant, moderate conductivity. It is acknowledged that some biogeochemical reactions, including those associated with biodegradation, occurring within the contaminant plume emanating from a DNAPL source zone may raise groundwater conductivity. Such reactions may increase the water-DNAPL electrical contrast when substantial DNAPL remains but may also complicate the mapping of DNAPL disappearance if bulk resistivity is decreasing due to both effects concurrently. Future simulations will examine this by prescribing elevated groundwater conductivity where dissolved phase solvent is present in the subsurface. Moreover, the model, which can simulate biodegradation directly, can be enhanced further in future to link degradation by-products to groundwater conductivity directly to evaluate the potential impacts of these transformations on the ability of ERT to track DNAPL remediation.

With respect to the presented linkage methodology, this work considers clayey-sand mixtures in which the maximum volume of clay added to the model domain is constrained by the porosity of sand; however, this is not considered a restrictive constraint for many materials relevant to hydrogeologic studies. Each of the published relationships associated with the linkage methodology has been independently validated against experimental data. However, it is acknowledged that the presented model as a whole has not been validated against experiments, and potential uncertainties may exist in the underlying petrophysical relationships or their cumulative predictions.

CONCLUSIONS

A numerical model was presented that creates a novel and robust link between a multiphase flow model, which generates realistic DNAPL release scenarios, and an ERT model, which simulates the corresponding resistivity response. Sensitivity studies and a field-scale simulation demonstrated the performance of the model and its sensitivity to variations in DNAPL distribution and subsurface heterogeneity. Results suggested that the coupled model can be a valuable and reliable research tool and provide a cost-effective means to develop and evaluate optimum ERT data acquisition, inversion, and interpretative tools for contaminated sites. This initial study will be a basis for future work, concentrating on (1) site characteristics most suited to ERT success, (2) detailed time-lapse monitoring of DNAPL remediation, (3) validating the synthetic ERT data with field results, and (4) extending the work to examine the benefits of complementary geoelectrical surveys.

ACKNOWLEDGMENTS

The authors would like to thank C. Berg and A. Revil for some helpful discussions on petrophysical relationships, as well as B. Giroux and two anonymous reviewers for their constructive comments and valuable suggestions for the article. The authors also acknowledge the financial support of the National Sciences and Engineering Research Council in the form of a Discovery Grant to the second author and an Industrial Postgraduate Scholarship to the first author, supported with industrial contributions from Geosyntec Consultants Ltd.

NOMENCLATURE

k	=	Hydraulic permeability (m^2)
k_{sd}	=	Hydraulic permeability of sand (m^2)
ϕ	=	Porosity
ϕ_{sd}	=	Porosity of sand
ϕ_{cl}	=	Porosity of clay
$\phi_{i,j}$	=	Porosity for increment i at disperse element j
ϕ_t	=	Total water volume
d_{sd}	=	Mean grain diameter of sand (m)
m_{sd}	=	Cementation exponent of sand
m_{cl}	=	Cementation exponent of clay
m_{cs}	=	Cementation exponent of clayey sand
m_j	=	Exponent of disperse element j
n	=	Saturation exponent
Cl	=	Volumetric clay content
V_{cl}	=	Bulk volume fraction of clay
V_{sd}	=	Bulk volume fraction of sand
V_w	=	Bulk volume fraction of water
V_d	=	Bulk volume fraction of DNAPL
V_a	=	Bulk volume fraction of air
$V_{i,j}$	=	Volume sum at increment i and disperse element j
V_{p}	=	Bulk volume of each respective disperse element j
V_j	=	Bulk volume of disperse element j
i, j	=	Subscripts for increments and disperse elements, respectively

S_w = Water saturation
S_d = DNAPL saturation
T = Temperature of pore water (°C)
C_f = Ionic concentration (mol/L) associated with salinity
ρ_w = Electrical resistivity of pore water (ohm-m)
σ_o^* = Complex mixture conductivity (S/m)
σ_w^* = Complex water conductivity (S/m)
σ_m^* = Complex matrix conductivity (S/m)
$\sigma_{o_{i,j}}$ = Electrical conductivity of the mixture at increment i and disperse element j (S/m)
σ_{d_j} = Electrical conductivity of disperse element j (S/m)
q = Number of disperse elements
s = Number of incremental steps

REFERENCES

Alexandra, R., J. I. Gerhard, and B. H. Kueper, 2012, Hydraulic displacement of dense, nonaqueous phase liquids for source zone stabilization: Ground Water, **50**, 765–774, doi: 10.1111/j.1745-6584.2011.00907.x.

Archie, G. E., 1942, The electrical resistivity log as an aid in determining some reservoir characteristics: Transactions of the AIME, **146**, 54–62, doi: 10.2118/942054-G.

Atekwana, E. A., E. Atekwana, F. D. Legall, and R. V. Krishnamurthy, 2005, Biodegradation and mineral weathering controls on bulk electrical conductivity in a shallow hydrocarbon contaminated aquifer: Journal of Contaminant Hydrology, **80**, 149–167, doi: 10.1016/j.jconhyd.2005.06.009.

Atekwana, E. A., and E. A. Atekwana, 2009, Geophysical signature of microbial activity at hydrocarbon contaminated sites: A review: Surveys in Geophysics, **31**, 247–283, doi: 10.1007/s10712-009-9089-8.

Attinger, S., J. Dimitrova, and W. Kinzelbach, 2009, Homogenization of the transport behavior of nonlinearly adsorbing pollutants in physically and chemically heterogeneous aquifers: Advances in Water Resources, **32**, 767–777, doi: 10.1016/j.advwatres.2009.01.011.

Bear, J., 1972, Dynamics of fluids in porous media: Dover.

Berg, C., 2007, An effective medium algorithm for calculating water saturations at any salinity or frequency: Geophysics, **72**, no. 2, E59–E67 doi: 10.1190/1.2432261.

Berg, C. R., 1995, A simple effective-medium model for water saturation in porous rocks: Geophysics, **60**, 1070–1080, doi: 10.1190/1.1443835.

Brewster, M. L., and A. P. Annan, 1994, Ground-penetrating radar monitoring of a controlled DNAPL release: 200 MHz radar: Geophysics, **59**, 1211–1221, doi: 10.1190/1.1443679.

Brewster, M. L., A. P. Annan, J. P. Greenhouse, B. H. Kueper, and G. R. Olhoeft, 1995, Observed migration of a controlled DNAPL release by geophysical methods: Ground Water, **33**, 977–987, doi: 10.1111/j.1745-6584.1995.tb00043.x.

Bruggeman, D.A.G., 1935, The calculation of various physical constants of heterogeneous substances. Part I: The dielectric constants and conductivities of mixtures composed of isotropic substances: Annalen der Physik, **416**, 636–664 (in German), doi: 10.1002/andp.19354160705.

Bussain, A. E., 1983, Electrical conductance in a porous medium: Geophysics, **48**, 1258–1268, doi: 10.1190/1.1441549.

Cardarelli, E., and G. Di Filippo, 2009, Electrical resistivity and induced polarization tomography in identifying the plume of chlorinated hydrocarbons in sedimentary formation: A case study in Rho (Milan - Italy): Waste Management and Research, **27**, 595–602, doi: 10.1177/0734242X09102524.

Chambers, J. E., M. H. Loke, R. D. Ogilvy, and P. I. Meldrum, 2004, Noninvasive monitoring of DNAPL migration through a saturated porous medium using electrical impedance tomography: Journal of Contaminant Hydrology, **68**, 1–22, doi: 10.1016/S0169-7722(03)00142-6.

Chambers, J. E., P. B. Wilkinson, G. P. Wealthall, M. H. Loke, R. Dearden, R. Wilson, D. Allen, and R. D. Ogilvy, 2010, Hydrogeophysical imaging of deposit heterogeneity and groundwater chemistry changes during DNAPL source zone bioremediation: Journal of Contaminant Hydrology, **118**, 43–61, doi: 10.1016/j.jconhyd.2010.07.001.

Cosenza, P., A. Ghorbani, C. Camerlynck, F. Rejiba, R. Guérin, and A. Tabbagh, 2009, Effective medium theories for modeling the relationships between electromagnetic properties and hydrological variables: A review: Near Surface Geophysics, **7**, 563–578, doi: 10.3997/1873-0604.2009009.

Daily, W., and A. Ramirez, 1995, Electrical resistance tomography during in-situ trichloroethylene remediation at the Savannah River Site: Journal of Applied Geophysics, **33**, 239–249, doi: 10.1016/0926-9851(95)90044-6.

Dekker, T. J., and L. M. Abriola, 2000, The influence of field-scale heterogeneity on the surfactant-enhanced remediation of entrapped nonaqueous phase liquids: Journal of Contaminant Hydrology, **42**, 219–251, doi: 10.1016/S0169-7722(99)00091-1.

de Lima, O. A. L., and M. M. Sharma, 1990, A grain conductivity approach to shaly sandstones: Geophysics, **55**, 1347–1356, doi: 10.1190/1.1442782.

Dhu, T., and G. Heinson, 2004, Numerical and laboratory investigations of electrical resistance tomography for environmental monitoring: Exploration Geophysics, **35**, 33–40, doi: 10.1071/EG04033.

Freeze, R. A., and J. A. Cherry, 1979, Groundwater: Prentice Hall.

Gerhard, J. I., and B. H. Kueper, 2003a, Capillary pressure characteristics necessary for simulating DNAPL infiltration, redistribution, and immobilization in saturated porous media: Water Resources Research, **39**, 1212, doi: 10.1029/2002WR001270.

Gerhard, J. I., and B. H. Kueper, 2003b, Relative permeability characteristics necessary for simulating DNAPL infiltration, redistribution, and immobilization in saturated porous media: Water Resources Research, **39**, 1213, doi: 10.1029/2002WR001490.

Gerhard, J. I., and B. H. Kueper, 2003c, Influence of constitutive model parameters on the predicted migration of DNAPL in heterogeneous porous media: Water Resources Research, **39**, 1279, doi: 10.1029/2002WR001570.

Gerhard, J. I., B. H. Kueper, G. R. Hecox, and R. Schwarz, 2001, Site-specific design for dual phase recovery and stabilization of pooled DNAPL: Ground Water Monitoring and Remediation, **21**, 71–88, doi: 10.1111/j.1745-6592.2001.tb00303.x.

Gerhard, J. I., T. Pang, and B. H. Kueper, 2007, Time scales of DNAPL migration in sandy aquifers: Ground Water, **45**, 147–157, doi: 10.1111/j.1745-6584.2006.00269.x.

Giroux, B., and M. Chouteau, 2008, A hydrogeophysical synthetic model generator: Computers & Geosciences, **34**, 1080–1092, doi: 10.1016/j.cageo.2007.11.006.

Grant, G. P., and J. I. Gerhard, 2007a, Simulating the dissolution of a complex dense non-aqueous phase liquid source zone. Part 1: Model to predict interfacial area: Water Resources Research, **43**, W12410, doi: 10.1029/2007WR006038.

Grant, G. P., and J. I. Gerhard, 2007b, Simulating the dissolution of a complex dense non-aqueous phase liquid source zone. Part 2: Experimental validation of an interfacial area-based mass transfer model: Water Resources Research, **43**, W12409, doi: 10.1029/2007WR006039.

Grant, G. P., J. I. Gerhard, and B. H. Kueper, 2007, Field scale impacts of spatially correlated relative permeability in heterogeneous multiphase systems: Advances in Water Resources, **30**, 1144–1159, doi: 10.1016/j.advwatres.2006.10.005.

Hanai, T., 1960, Theory of the dielectric dispersion due to the interfacial polarization and its application to emulsions: Kolloid-Zeitschrift, **171**, 23–31, doi: 10.1007/BF01520320.

Hanai, T., 1961, A remark on "Theory of the dielectric dispersion due to the interfacial polarization and its application to emulsions": Kolloid-Zeitschrift, **175**, 61–62, doi: 10.1007/BF01520118.

Illangasekare, T. H., J. L. Ramsey, Jr., K. H. Jensen, and M. B. Butts, 1995, Experimental study of the movement and distribution of dense organic contaminants in heterogeneous aquifer: Journal of Contaminant Hydrology, **20**, 1–25, doi: 10.1016/0169-7722(95)00045-W.

Karaoulis, M. C., J. H. Kim, and P. I. Tsourlos, 2011a, 4D active time constrained resistivity inversion: Journal of Applied Geophysics, **73**, 25–34, doi: 10.1016/j.jappgeo.2010.11.002.

Karaoulis, M., A. Revil, D. D. Werkema, B. J. Minsley, W. F. Woodruff, and A. Kemna, 2011b, Time-lapse three-dimensional inversion of complex conductivity data using an active time constrained (ATC) approach: Geophysical Journal International, **187**, 237–251, doi: 10.1111/j.1365-246X.2011.05156.x.

Kavanaugh, M. C., P. S. C. Rao, L. Abriola, C. Newell, J. Cherry, T. Sale, G. Destouni, S. Shoemaker, R. Falta, R. Siegrist, D. Major, G. Teutsch, J. Mercer, and K. Udell, 2003, The DNAPL remediation challenge: Is there a case for source depletion?: United States Environmental Protection Agency.

Kim, J. H., and M. J. Yi, 2010, DC_3DPro: User's manual: Geoelectric Imaging Laboratory: Korea Institute of Geoscience and Mineral Resources.

Kim, J. H., M. J. Yi, S. G. Park, and J. G. Kim, 2009, 4-D inversion of DC resistivity monitoring data acquired over a dynamically changing earth model: Journal of Applied Geophysics, **68**, 522–532, doi: 10.1016/j.jappgeo.2009.03.002.

Kueper, B. H., and K. L. Davies, 2009, Assessment and delineation of DNAPL source zones at hazardous waste sites: United States Environmental Protection Agency, Publication EPA/600/R-09/119.

Kueper, B. H., and J. I. Gerhard, 1995, Variability of point source infiltration rates for two-phase flow in heterogeneous porous media: Water Resources Research, **31**, 2971–2980, doi: 10.1029/95WR02329.

Kueper, B. H., J. D. Redman, R. C. Starr, S. Reitsma, and M. Mah, 1993, A field experiment to study the behavior of tetrachloroethylene below the

water table: Spatial distribution of residual and pooled DNAPL: Ground Water, **31**, 756–766, doi: 10.1111/j.1745-6584.1993.tb00848.x.
Kueper, B. H., G. P. Wealthall, J. W. N. Smith, S. A. Leharne, and D. N. Lerner, 2003, An illustrated handbook of DNAPL transport and fate in the subsurface: Environment Agency R&D Publication.
Loke, M. H., 2010, Tutorial: 2-D and 3-D electrical imaging surveys, http://www.geotomosoft.com/downloads.php, accessed 12 July 2012.
Lucius, J. E., G. R. Olhoeft, P. L. Hill, and S. K. Duke, 1992, Properties and hazards of 108 selected substances – 1992 edition: Open-File Report, 92-527, U.S. Geological Survey.
Marion, D., A. Nur, H. Yin, and D. Han, 1992, Compressional velocity and porosity in sand-clay mixtures: Geophysics, **57**, 554–563, doi: 10.1190/1.1443269.
Mercer, J. W., and R. M. Cohen, 1990, A review of immiscible fluids in the subsurface: Properties, models, characterization, and remediation: Journal of Contaminant Hydrology, **6**, 107–163, doi: 10.1016/0169-7722(90)90043-G.
Nenna, V., A. Pidlisecky, and R. Knight, 2011, Informed experimental design for electrical resistivity imaging: Near Surface Geophysics, **9**, 469–482, doi: 10.3997/1873-0604.2011027.
Newmark, R. L., W. D. Daily, K. R. Kyle, and A. L. Ramirez, 1998, Monitoring DNAPL pumping using integrated geophysical techniques: Journal of Environmental and Engineering Geophysics, **3**, 7–13, doi: 10.4133/JEEG3.1.7.
Ogilvy, R. D., O. Kuras, P. I. Meldrum, P. B. Wilkinson, J. E. Chambers, M. Sen, A. Pulido-Bosch, J. Gisbert, S. Jorreto, I. Frances, and P. Tsourlos, 2009, Automated monitoring of coastal aquifers with electrical resistivity tomography: Near Surface Geophysics, **7**, 367–375, doi: 10.3997/1873-0604.2009027.
Pang, T. W., J. I. Gerhard, M. West, and B. H. Kueper, 2007, Numerical simulation of ISCO to remediate DNAPL in fractured rock: Proceedings of the 2007 U.S. EPA/NGWA Fractured Rock Conference: State of the Science and Measuring Success in Remediation, 133–147.
Papadopoulos, N. G., P. Tsourlos, C. Papazachos, G. N. Tsokas, A. Sarris, and J. H. Kim, 2011, An algorithm for fast 3D inversion of surface electrical resistivity tomography data: Application on imaging buried antiquities: Geophysical Prospecting, **59**, 557–575, doi: 10.1111/j.1365-2478.2010.00936.x.
Papadopoulos, N. G., P. Tsourlos, G. N. Tsokas, and A. Sarris, 2006, Two-dimensional and three-dimensional resistivity imaging in archaeological site investigation: Archeological Prospection, **13**, 163–181, doi: 10.1002/arp.276.
Papadopoulos, N. G., P. Tsourlos, G. N. Tsokas, and A. Sarris, 2007, Efficient ERT measuring and inversion strategies for 3D imaging of buried antiquities: Near Surface Geophysics, **5**, 349–362, doi: 10.3997/1873-0604.2007017.
Redman, J. D., 2009, Contaminant mapping, in H. M. Jol, ed., Ground penetrating radar: Theory and applications: Elsevier, 247–269.
Revil, A., 2012, Spectral induced polarization of shaly sands: Influence of the electrical double layer: Water Resources Research, **48**, W02517, doi: 10.1029/2011WR011260,2012.
Revil, A., and L. M. Cathles, 1999, Permeability of shaly sands: Water Resources Research, **35**, 651–662, doi: 10.1029/98WR02700.
Revil, A., L. M. Cathles, III, S. Losh, and J. A. Nunn, 1998, Electrical conductivity in shaly sands with geophysical applications: Journal of Geophysical Research, **103**, 23.925–23.936, doi: 10.1029/98JB02125.
Robin, M. J. L., E. A. Sudicky, R. W. Gillham, and R. G. Kachanowski, 1991, Spatial variability of strontium distribution coefficients and their correlation with hydraulic conductivity in the Canadian Forces Base Borden aquifer: Water Resources Research, **27**, 2619–2632, doi: 10.1029/91WR01107.
Sauck, W. A., 2000, A model for the resistivity structure of LNAPL plumes and their environs in sandy sediments: Journal of Applied Geophysics, **44**, 151–165, doi: 10.1016/S0926-9851(99)00021-X.
Sauck, W. A., E. A. Atekwana, and M. S. Nash, 1998, Elevated conductivities associated with an LNAPL plume imaged by integrated geophysical techniques: Journal of Environmental and Engineering Geophysics, **2**, 203–212.
Schön, J. H., 1996, Physical properties of rocks — Fundamentals and principles of petrophysics, Handbook of geophysical exploration, Seismic exploration, Vol. 18: Elsevier Science Ltd.
Schön, J. H., and D. T. Georgi, 2003, Dispersed shale, shaly-sand permeability — A hydraulic analog to the Waxman-Smits equation: Presented at SPWLA 44th Annual Logging Symposium.
Sen, P. N., and P. A. Goode, 1992, Influence of temperature on electrical conductivity on shaly sands: Geophysics, **57**, 89–96, doi: 10.1190/1.1443191.
Slater, L., 2007, Near surface electrical characterization of hydraulic conductivity: From petrophysical properties to aquifer geometries — A review: Surveys in Geophysics, **28**, 169–197, doi: 10.1007/s10712-007-9022-y.
Sudicky, E. A., W. A. Illman, I. K. Goltz, J. J. Adams, and R. G. McLaren, 2010, Heterogeneity in hydraulic conductivity and its role on the macroscale transport of a solute plume: From measurements to a practical application of stochastic flow and transport theory: Water Resources Research, **46**, W01508, doi: 10.1029/2008WR007558.
Tsourlos, P., and R. Ogilvy, 1999, An algorithm for the 3-D inversion of tomographic resistivity and induced polarization data: Preliminary results: Journal of the Balkan Geophysical Society, **2**, 30–45.
Waxman, M. H., and L. J. M. Smits, 1968, Electrical conductivities and oil-bearing shaly sands: Society of Petroleum Engineers Journal, **8**, 107–122, doi: 10.2118/1863-A.
West, M. R., G. P. Grant, J. I. Gerhard, and B. H. Kueper, 2008, The influence of precipitate formation on the chemical oxidation of TCE DNAPL with potassium permanganate: Advances in Water Resources, **31**, 324–338, doi: 10.1016/j.advwatres.2007.08.011.
Wilson, V. C., C. Power, A. Giannopoulos, J. I. Gerhard, and G. P. Grant, 2009, DNAPL mapping by ground penetrating radar examined via numerical simulation: Journal of Applied Geophysics, **69**, 140–149, doi: 10.1016/j.jappgeo.2009.08.006.
Yi, M. J., J. H. Kim, and S. H. Chung, 2003, Enhancing the resolving power of least-squares inversion with active constraint balancing: Geophysics, **68**, 931–941, doi: 10.1190/1.1581045.
Yi, M. J., J. H. Kim, Y. Song, S. J. Cho, S. H. Chung, and J. H. Suh, 2001, Three-dimensional imaging of subsurface structures using resistivity data: Geophysical Prospecting, **49**, 483–497, doi: 10.1046/j.1365-2478.2001.00269.x.
Zhou, Q. Y., J. Shimada, and A. Sato, 2001, Three-dimensional spatial and temporal monitoring of soil water content using electrical resistivity tomography: Water Resources Research, **37**, 273–285, doi: 10.1029/2000WR900284.